PHYSICAL REVIEW B VOLUME 15, NUMBER 4 15 FEBRUARY 1977

Anisotropic quasiparticle properties in aluminum*

A. B. Meador† and W. E. Lawrence
Department of Physics, Dartmouth College, Hanover, New Hampshire 03755
(Received 12 October 1976)

We have studied the electron-phonon interaction in aluminum using Fermi-surface-fitted 4-orthogonalized-plane-wave electron states, a realistic phonon spectrum, and integration mesh density varying with local Fermi-surface curvature. The resulting electron-mass enhancement λ and thermal scattering rate τ^{-1} are evaluated as functions of position on the Fermi surface, with the following results: (i) The agreement between observed and calculated cyclotron masses is improved slightly by the use of our anisotropic λ rather than the average one. (ii) The anisotropy of λ is determined predominantly by mixing coefficient variations, rather than by phonon anisotropy. (iii) The scattering rate τ^{-1} exhibits order-of-magnitude variations over the Fermi surface at low temperatures. Its values at 5 K are within 50% of the experimentally observed ones everywhere, with considerably better agreement in free-electron regions. (iv) Deviations from the naively expected T^3 behavior are predicted: In free-electron regions, umklapp processes cause a *more rapid* increase than T^3 for temperatures above 15–25 K. On ridges, where the initial "T^3 coefficient" is very large, we find a *slower* increase. There results a washing out of anisotropy with increasing temperature. The results on λ are in good agreement with those of a recent similar calculation; the τ^{-1} results agree qualitatively but not quantitatively.

I. INTRODUCTION

The continuing growth in capability to measure and analyze the scattering rates of quasiparticle excitations in metals[1,2] is exciting for a number of reasons, of which two are (i) the scattering rate τ^{-1}, together with the effective-mass enhancement λ, are basic to the description[3,4] of low-lying electronic excitations in the interacting electron-phonon system, and (ii) the quasiparticle rate τ^{-1} is a uniquely sensitive probe of the *anisotropy* of the electron-phonon interaction—anisotropy which manifests itself less directly in other quantities such as transport coefficients.[5] To amplify on the last statement, the electrical conductivity (for example) may be written as an average of the anisotropic transport relaxation time τ_{tr}. Although its anisotropy gives rise to dramatic effects, it cannot be measured directly, and at best only its qualitative features may be inferred from experimental data. So transport coefficients are rather insensitive probes of anisotropy.

In this paper we are concerned with the calculation of the quasiparticle properties, λ and τ, of aluminum. The reason for the choice is that aluminum presents the interesting combination of a multisheeted Fermi surface with a very simple electronic structure [its electronic properties, including Fermi-surface shape, are well described by Ashcroft's 4-OPW (orthogonalized-plane-wave) model[6]]. Because of this simplicity the nature of the electron states is intimately related to the Fermi-surface shape: single-OPW states in spherical regions, 2-OPW in most of the high-curvature regions (near zone boundaries), and 4-OPW near the zone corners. Certain features of the quasiparticle properties might therefore be dictated by the surface shape.

The ingredients in this calculation are discussed in detail in Sec. II, and so we state them only briefly here for comparison with previous calculations. The 4-OPW model is used for both the Fermi-surface shape and the electron-phonon matrix elements, and a realistic phonon spectrum is used as well for the latter. The quasiparticle quantities are then calculated by direct integration over the Fermi surface, using a fixed mesh whose point density is determined by local Fermi-surface curvature. This calculational program and a somewhat similar one by Leung[7] differ from all previous aluminum calculations[8] in their detailed treatment of the electron structure. This program differs from Leung's in two respects: (a) Leung uses 15-OPW electron states and the Heine-Abarenkov pseudopotential for the calculation of matrix elements; (b) rather than doing surface integrals directly, he introduces the frequency distribution functions $\alpha^2F(\vec{k}, \omega)$ as an intermediate step.[7,8] The general agreement between our calculated values of λ suggests that the matrix elements are not seriously affected by the use of one method over the other. The discrepancy which exists between the τ values probably arises from the difference between our integration methods, since it is difficult in either case to treat low-frequency phonons with a high degree of accuracy. This problem will be discussed at length later.

In the remainder of this section we review the surface-integral expressions for λ and τ. First consider the simpler quanity λ; recall that it relates the quasiparticle velocity

$$\vec{v}_Q(\vec{k}) = [1+\lambda(\vec{k})]^{-1}\vec{v}(\vec{k}) \tag{1}$$

to the bare "band" velocity $\vec{v}(\vec{k})$. It is given by the Fermi-surface integral[3]

$$\lambda(\vec{k}) = \frac{1}{4\pi^3}\int \frac{dS'}{\hbar|\vec{v}'|}\sum_\sigma \frac{|g_\sigma(\vec{k},\vec{k}')|^2}{\omega_{q\sigma}}, \tag{2}$$

where

$$|g_\sigma(\vec{k},\vec{k}')|^2 = (2\rho\omega_{q\sigma})^{-1}|\langle\vec{k}'|\hat{\epsilon}_{q\sigma}\cdot\nabla V|\vec{k}\rangle|^2 \tag{3}$$

is the squared amplitude for the electron transition $\vec{k}\to\vec{k}'$, with the emission or absorption of a phonon with wave vector $\vec{q}$ and polarization σ (for an emitted phonon, $\vec{q}=\vec{k}-\vec{k}'$ reduced to the first Brillouin zone). In (3), ρ is the mass density of aluminum, V is the Ashcroft pseudopotential (for consistency with the Fermi-surface fit), and of course $\omega_{q\sigma}$ and $\hat{\epsilon}_{q\sigma}$ are the phonon frequency and polarization, respectively. A similar formula holds for the thermal quasiparticle relaxation rate at the Fermi surface ($\epsilon=0$, Ref. 3)

$$\tau^{-1}(\vec{k},\epsilon=0) = \frac{1}{\pi^2}\int \frac{dS'}{\hbar|\vec{v}'|}\sum_\sigma |g_\sigma(\vec{k},\vec{k}')|^2 f(\hbar\omega_{q\sigma}/k_BT), \tag{4}$$

where

$$f(x) = (e^x-1)^{-1}(1+e^{-x})^{-1}$$
$$\equiv n(x)[1-f^0(x)]$$

incorporates the temperature dependence through the equilibrium Fermi and Bose functions f^0 and n; note that $f(x)$ falls off exponentially for large x. For quasiparticles *off* the Fermi surface the relaxation rate $\tau^{-1}(\vec{k},\epsilon)$ is slightly more complicated than (4). For the measurements done in aluminum[9] the appropriate quantity is the *average* of $\tau^{-1}(\vec{k},\epsilon)$ over energies near the Fermi level, as discussed in a number of places,[4,10] and that is simply

$$\langle\tau^{-1}(\vec{k})\rangle \equiv \int_{-\infty}^{\infty} d\epsilon\left(-\frac{\partial f^0(\epsilon)}{\partial\epsilon}\right)\tau^{-1}(\vec{k},\epsilon)$$
$$= \tfrac{12}{7}\,\tau^{-1}(\vec{k},\epsilon=0) \tag{5}$$

related to the value *at* the Fermi level. Later we compare experimental measurements with $\langle\tau^{-1}(\vec{k})\rangle$, (5), rather than (4).

One further point must be discussed here. For very low temperatures the occupation factors $f(x)$ restrict important contributions to the integral in (4) to the immediate vicinity of $\vec{k}$ (i.e., $|\vec{k}'-\vec{k}|\ll k_F$). The result is that, for any fixed integration mesh, the numerical sum intended to represent (4) approaches zero exponentially [$\exp(-c/T)$], rather than algebraically (T^3) as does the exact integral (4), in the limit $T\to 0$. However, the exact low-temperature limit may be calculated by writing the surface integral in plane polar coordinates

$$dS' \to q\,dq\,d\theta \quad (T\to 0)$$

and observing the asymptotic form

$$\lim_{\vec{k}'\to\vec{k}}\frac{|g_\sigma(\vec{k},\vec{k}')|^2}{\omega_{q\sigma}} \equiv \lim_{\vec{k}'\to\vec{k}} G_\sigma(\vec{k},\vec{k}') = G_\sigma(\theta), \tag{6}$$

(this independence of G_σ on q will be demonstrated explicitly later) which permits the integrals to factorize. It is then elementary to show that

$$\lim_{T\to 0}\tau^{-1}(\vec{k},\epsilon=0) = \frac{2.104}{\pi^2\hbar^4|\vec{v}|}(k_BT)^3 \times\int_0^{2\pi} d\theta\sum_\sigma G_\sigma(\theta)C_\sigma^{-2}(\theta), \tag{7}$$

where $C_\sigma(\theta)$ is defined by $\lim_{q\to 0}\omega_{q\sigma}(\theta) = qC_\sigma(\theta)$. The angular integral may be done numerically, to provide the exact T^3 coefficient for the low-temperature limit. This procedure will be discussed further in Sec. II, along with many other details of the computations. The results of the calculations of both λ and τ^{-1} are given in Sec. III.

II. CALCULATIONS

In this section we describe the method used to perform the Fermi-surface integrations required in (2), (4), and (7), and we discuss the calculation of the necessary ingredients in the integrands. The integration mesh is shown on Fig. 1. It consists of 1294 points: 873 on the second zone hole surface, and 421 on the third zone electron surface. The mesh-point density is greatest near the zone edges, where the curvature is high; the density was chosen to satisfy a criterion based on the electron-phonon matrix element variation (to be discussed later). It is apparent that the density is sufficient to represent the Fermi-surface shape adequately. The points are located, *and* the wave functions are calculated by means of Ashcroft's 4-OPW model. This model provides an excellent fit to the actual Fermi-surface shape,[6] and we believe that it gives the wave functions to a sufficiently high level of accuracy that they are not a limiting factor in the overall accuracy of the calculation.

For each mesh point, we calculate the element of surface area and the velocity $\vec{v}=\hbar^{-1}\vec{\nabla}_k\epsilon$. These are then used to evaluate three surface integrals of interest, two of which are related to the "specific heat" and "optical" effective masses, as shown in Table I.

The matrix elements (3) required for the quasiparticle properties are calculated using the 4-OPW wave functions of the Ashcroft model, and a phonon spectrum derived from a Born–von Kármán force-constant fit to neutron data. The rationale for using the simple 4-OPW model for the matrix ele-

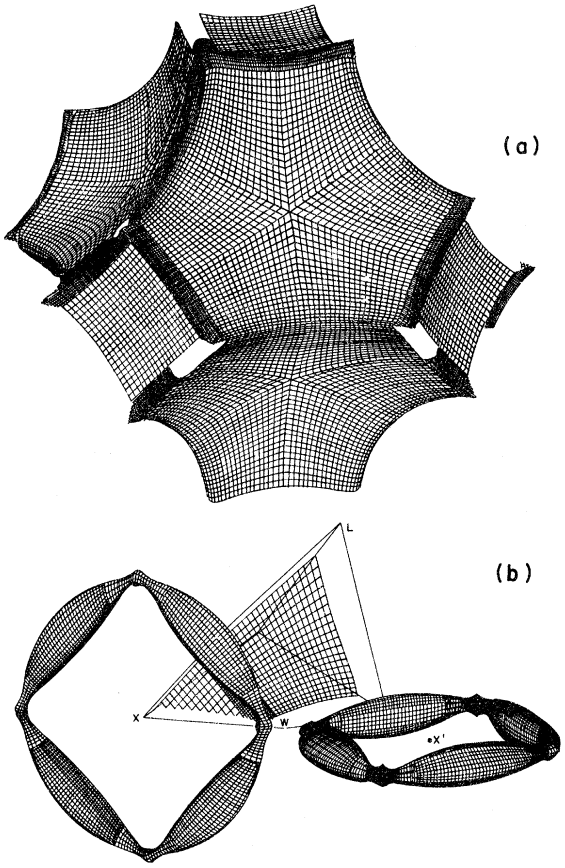

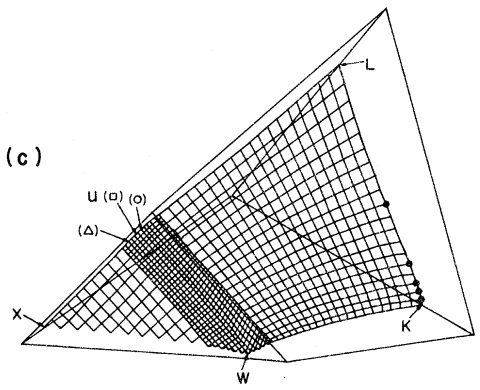

FIG. 1. (a) Second-zone Fermi surface. (b) Second-and third-zone Fermi-surface sheets shown together. The $\frac{1}{48}$th minimum symmetry element is shown for the second zone; the third zone consists of three such sets of arms. (c) Second-zone mesh shown in detail. Certain Fermi-surface points are named after corresponding points of high symmetry in the zone. The point U is defined so that its normal is $\hat{x}$ directed, to enable later comparison with experiment. Unnamed points, indicated by dots, will also be referred to later.

ments is as follows: First, we recall that Ashcroft's model is empirical, in the sense that the measured Fermi-surface dimensions are used to infer the band gaps $V(G)$. These band gaps are the values of the electron-ion form factor at the reciprocal lattice points $\vec{G}=[111]$ and $\vec{G}=[200]$. The form factor represents the electron-ion pseudopotential operator V—the same V which occurs in the electron-phonon matrix elements (3). For consistency, then, the matrix elements should be calculated from a pseudopotential which "reproduces" Ashcroft's empirical band gaps, and from the same 4-OPW wave functions used in their determination.

In connection with the choice of form factor, we should point out that the usual Ashcroft form[11] is used, but with the ionic core parameter R_c set at 0.61 Å, rather than the 0.59 Å quoted in Ref. 11. This choice is necessary in order to fit the empirical band gaps; it fits V_1 essentially exactly and overestimates V_2 by 13%. In contrast, the choice $R_c=0.60$ Å underestimates V_1 seriously (~35%), while $R_c=0.62$ Å overestimates both V_1 and V_2.

We have studied extensively the variation of the quantity $G_\sigma(\vec{k},\vec{k}')\equiv\omega_{q\sigma}^{-1}|g_\sigma(\vec{k},\vec{k}')|^2$ [the integrand of λ, see Eq. (2)] over the Fermi surface, particularly in the vicinity of ridges. Through this study we developed the criterion for mesh density that the quantity $G_\sigma(\vec{k},\vec{k}')$ should vary by no more than 10% under the displacement of its arguments by a single interval in any direction. This criterion supplements the more subjective one that the mesh

TABLE I. Listed are our computed values of surface integrals representing the "specific-heat" and "optical" effective masses, and the Fermi-surface area. The free-electron velocity v_0 and surface area S_0 are given for reference. Free-electron quantities: $v_0=2.02\times10^8$ cm/sec; $S_0=38.5$ Å^{-2}.

Surface integral	Computed value
$\frac{m_{SH}}{m}=\frac{v_0}{S_0}\int\frac{dS}{\lvert\vec{v}\rvert}$	0.986
$S_0^{-1}\int dS$	0.79
$\frac{m}{m_{opt}}=(S_0v_0)^{-1}\int dS\lvert\vec{v}\rvert$	0.67

accurately represent the Fermi-surface shape. As a result, there are relatively small regions, near the centers of ridges, where the 10% criterion becomes the determining factor for mesh density. The highest density is required near the narrow ridge which (on the second zone surface) joins the hexagonal and square regions. We call this the "V_1-ridge" since it is determined by the smaller of the two band gaps, $V_1 \equiv V(\vec{G}=[111])$. The wider "$V_2$-ridge" $V_2 \equiv V(\vec{G}=[200])$ joins two hexagonal regions of the second zone, and requires mesh-density only slightly greater than that used in free-electron (1-OPW) regions near L and X. The third zone arms of the Fermi surface consist largely of ridges, and therefore they require dense mesh everywhere; as a result, the third zone accounts for roughly one-third of the total number of mesh points (see Fig. 2).

Although the 10% criterion is important only near the ridges, it is still responsible for the large number of mesh points, because so many of them (about two-thirds of the total number) occur near ridges. The mesh pictured in Figs. 1 and 2 is ultimately a compromise between accuracy (10% criterion), computer run-time (to compute λ at a single point requires about 3000 sec), and program cumbersomeness (the mesh consists of seven separate regions—three on the second zone and four on the third zone).

Now we return to the point raised at the conclusion of Sec. I—the problem of calculating τ^{-1} at very low temperatures. When typical thermally occupied phonon wave vectors are comparable with or smaller than the mesh-point separations, the strict mesh-summation no longer represents the integral (3). However, in the low-temperature limit, τ^{-1} depends only on the *gradients* of the mixing coefficients (evaluated at the initial point $\vec{k}$), and on the directional sound velocities $C_\sigma(\theta)$. These gradients may be evaluated with the use of the mesh points neighboring the initial state, and so the calculation is relatively simple. The actual expression for τ^{-1} in the low-temperature limit may be derived by expanding the matrix element in (3):

$$\frac{1}{i}\langle\vec{k}'|\hat{\epsilon}_{q\sigma}\cdot\nabla V|\vec{k}\rangle=\hat{\epsilon}_{q\sigma}\cdot\sum_{i=1}^{4}\sum_{j=1}^{4}\alpha_i\beta_j^*(\vec{k}-\vec{G}_i-\vec{k}'+\vec{G}_j)\times V(\vec{k}-\vec{G}_i-\vec{k}'+\vec{G}_j), \tag{8}$$

where α_i and β_j are the mixing coefficients of the 4-OPW states, e.g., $|\vec{k}\rangle=\sum_{i=1}^{4}|\alpha_i|\vec{k}-\vec{G}_i\rangle_0$, and $V(p)\equiv{}_0\langle\vec{q}|V|\vec{q}+\vec{p}\rangle_0$ is the matrix element of the (local) pseudopotential V between single-OPW states $|\vec{q}+\vec{p}\rangle_0$ and $|\vec{q}\rangle_0$. In the limit $\vec{k}'\to\vec{k}$ we are of course considering an intraband process, so that α_j and β_j have the same functional form $\alpha_j(\vec{k})$,

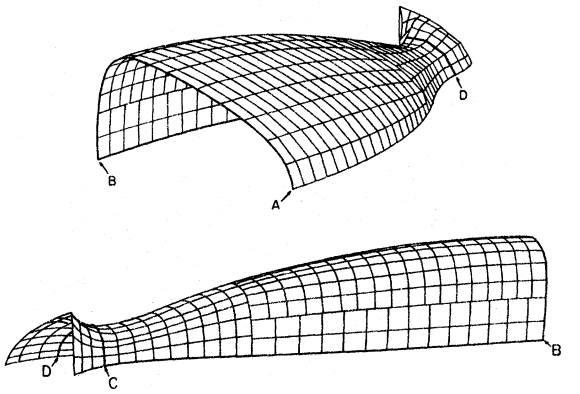

FIG. 2. Two views of the minimum-symmetry element of the third-zone surface. λ and τ^{-1} are later calculated along the indicated line segments.

and

$$\beta_j(\vec{k}')=\alpha_j(\vec{k})+(\vec{k}'-\vec{k})\cdot\nabla\alpha_j(\vec{k}). \tag{9}$$

Retaining only the lowest-order terms in the phonon wave vector $q=k-k'$ we end up with [neglecting the $\partial V(p)/\partial p$ term[12]]

$$\frac{1}{i}\langle\vec{k}'|\hat{\epsilon}_{q\sigma}\cdot\nabla V|\vec{k}\rangle=\hat{\epsilon}_{q\sigma}\cdot[\vec{q}\,V(0)+\sum_{i<j}\vec{A}_{ij}qV(\vec{G}_i-\vec{G}_j)], \tag{10a}$$

where

$$\vec{A}_{ij}=(\vec{G}_i-\vec{G}_j)(\alpha_i\nabla_q\alpha_j^*-\alpha_j\nabla_q\alpha_i^*), \tag{10b}$$

and ∇_q is the component of the gradient (in $\vec{k}$ space) in the $\vec{q}$ direction. We may now insert (10) into (3), and use $\lim_{q\to0}\omega_{q\sigma}=qC_\sigma(\hat{q})$ to write

$$\lim_{\vec{k}'\to\vec{k}}G_\sigma(\vec{k},\vec{k}')=\frac{1}{2\rho C_\sigma^2(\hat{q})}\left|\hat{\epsilon}_{q\sigma}\cdot\left(\hat{q}V(0)+\sum_{i<j}\vec{A}_{ij}V(G_i-G_j)\right)\right|^2, \tag{11}$$

[recall $G_\sigma(\vec{k},\vec{k}')\equiv\omega_{q\sigma}^{-1}|g_\sigma(\vec{k},\vec{k}')|^2$] which depends on the direction of $\vec{q}$ and not on its magnitude, as claimed in (6).

Now the form (11) is valid for points $\vec{k}'$ inside the element of surface area associated with the initial point $\vec{k}$, and so we may calculate *their* contribution $\tau_{\text{init}}^{-1}(\vec{k})$ to the integral (4) for $\tau^{-1}(\vec{k})$ to very good accuracy, in a manner analogous to the derivation of the zero-temperature limit (7). The difference is that the radial integral (dq) is now truncated at the surface-element boundary $q(\theta)$, and does not extend to infinity as in (7).

$$\tau^{-1}_{\text{init}}(\vec{k}, \epsilon = 0) = (\pi^2 \hbar |\vec{v}|)^{-1} \sum_\sigma \int_0^{2\pi} d\theta G_\sigma(\theta) C_\sigma(\theta) \int_0^{q(\theta)} q^2 \, dq \, f(\hbar\omega_q / k_B T) . \tag{12}$$

The radial integral may still of course be done analytically, and then the angular integral done numerically. As a result of the truncation $q(\theta)$, the contribution $\tau^{-1}_{\text{init}}(\vec{k})$ is accurate for all temperatures, and this guarantees that the total scattering rate

$$\tau^{-1}(\vec{k}, \epsilon = 0) = \tau^{-1}_{\text{init}}(\vec{k}, \epsilon = 0) + (\text{sum over all other mesh points } \vec{k}') \tag{13}$$

is accurate both at zero temperature [where $\tau^{-1} = \tau^{-1}_{\text{init}}$ are both equal to (7)] and at higher temperatures where typical phonon wave vectors are sufficiently large that the mesh provides adequate angular resolution. The expression (13) may not be accurate for some intermediate temperature interval, depending on the mesh density near $\vec{k}$. Evaluating τ^{-1} at 5-K intervals, we find apparent minor loss of accuracy only at 5 K, occuring at some of the Fermi-surface points.

III. RESULTS

A. Effective-mass enhancements

We first present results for the effective-mass enhancement λ, since it is the simpler quantity to talk about. λ is plotted in Fig. 3 as a function of position $\vec{k}$ on the Fermi surface, for orbits indicated on Figs. 1 and 2. Note that the values 0.37–0.42 are characteristic of free-electron-like regions, and that localized deviations from this range of values occur on the ridges. On the second-zone ridges the deviation is an increase; on third-zone ridges (near the principal section) it is a decrease. Near the third-zone neck the situation is more complicated and λ is untypically large everywhere. Our interpretation of the behavior everywhere except near the neck is that the localized deviations arise from changes in the electronic mixing coefficients. This is evidenced both by the localization to the ridges [the mixing coefficients are the only important quantities in (2) which

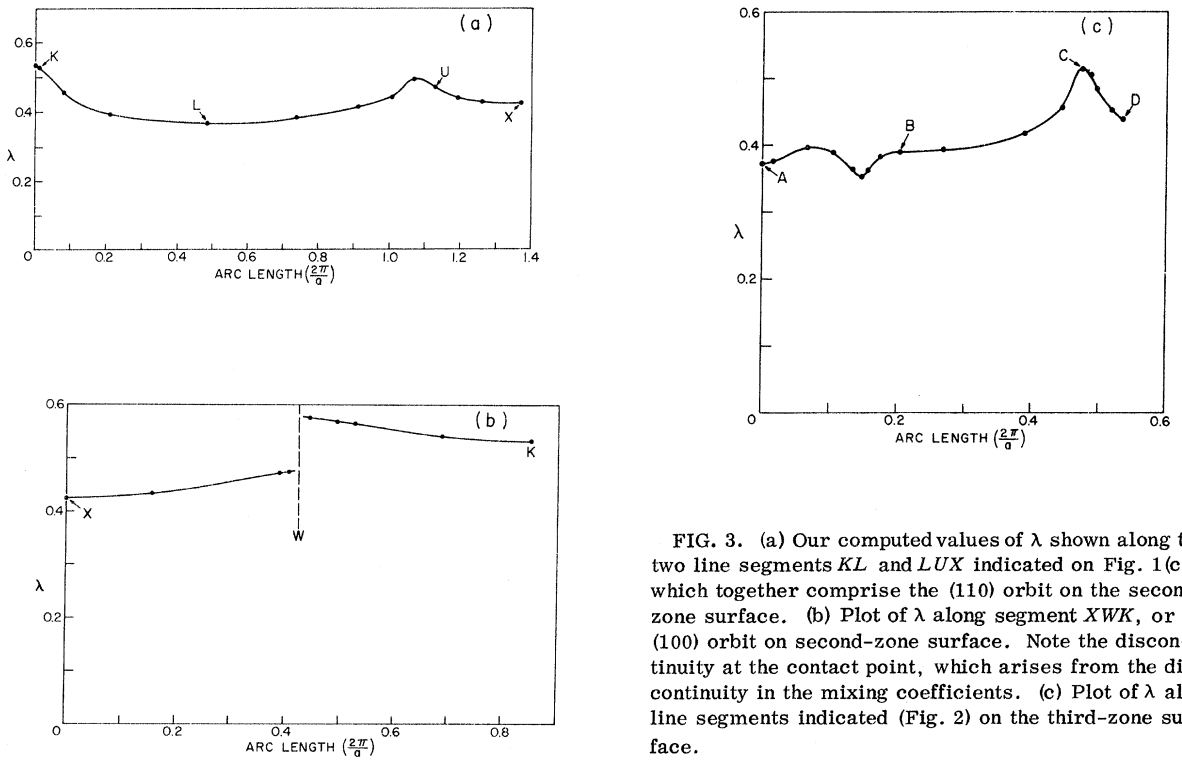

FIG. 3. (a) Our computed values of λ shown along the two line segments KL and LUX indicated on Fig. 1(c), which together comprise the (110) orbit on the second zone surface. (b) Plot of λ along segment XWK, or (100) orbit on second-zone surface. Note the discontinuity at the contact point, which arises from the discontinuity in the mixing coefficients. (c) Plot of λ along line segments indicated (Fig. 2) on the third-zone surface.

TABLE II. For various extremal orbits on the second and third zones, we list measured cyclotron masses, calculated "band" masses (unenhanced), "apparent" mass enhancements $\lambda(\text{apparent}) = m_c(\text{expt})/m_c(\text{calc}) - 1$, and the results of the present calculation $\lambda(\text{calc})$.

Orbit	m_c/m (expt)	m_c/m(calc) [b]	λ(apparent) [b]	m_c/m(calc) [c] (E-dependent pseudopotential)	λ(apparent) [c]	λ(calc)
Second zone						
(110) central orbit	$\frac{1.30 \pm 0.1^{a}}{1.27^{d}}$	0.822	$0.58 \pm 0.1^{a,b}$	0.87	$0.49 \pm 0.1^{a,c}$	0.42
(111) central orbit	$\frac{1.36 \pm 0.1^{a}}{1.40^{d}}$	0.902	$0.51 \pm 0.1^{a,b}$	0.95	$0.43 \pm 0.1^{a,c}$	0.42
Third zone						
(110) central arm	0.130 ± 0.004^{e}	0.0897	0.47 ± 0.01^{f}	0.095	$0.39 \pm 0.01^{f,c}$	0.38
	$\frac{0.132 \pm 0.001^{f}}{0.13^{d}}$					
(100) inner ring	$\frac{0.84 \pm 0.07^{a}}{0.80^{d}}$	0.495	$0.70 \pm 0.15^{a,b}$	0.52	$0.62 \pm 0.15^{a,c}$	0.44
(100) neck	0.091 ± 0.003^{e}			0.0605	$0.50 \pm 0.05^{e,c}$	0.48

[a] J. R. Anderson and S. S. Lane, Phys. Rev. B 2, 298 (1970).
[b] N. W. Ashcroft, Philos. Mag. 8, 2055 (1963), Ref. 6.
[c] N. W. Ashcroft, Ph.D. thesis (Cambridge Univ., 1964)(unpublished), Ref. 14.
[d] F. Spong and A. F. Kip, Phys. Rev. 137, A431 (1965).
[e] C. O. Larson and W. L. Gordon, Phys. Rev. 156, 703 (1967).
[f] R. T. Mina, V. S. Edelman, and M. S. Khaikin, Sov. Phys. JETP 24, 920 (1967).

vary on such a short scale], and by the antisymmetry between zones. The antisymmetry may be understood by first noting that near a given ridge, and sufficiently far away from the third-zone neck region, *two* of the four mixing coefficients are dominant in the wave functions. It follows that the product of the two dominant mixing coefficients on, say, a second-zone ridge, has the opposite sign from the corresponding product on the third-zone ridge. As a result, typical squared matrix elements in (3) exhibit opposite interference effects in the two zones, and these appear to be largely responsible for the localized deviations in λ.

In addition to these ridge-localized variations, there are also longer-range variations: λ is somewhat larger in the vicinity of X (the square region) that it is near L (the hexagonal region) on the second-zone surface. On the third-zone surface λ tends to become larger as one moves toward the neck region. These long-range variations seem to be related to the amount of umklapp scattering which can occur, from the region in question. The X region of the second zone generally lies closer to a zone boundary than does the L region, and so umklapp processes are available at smaller wave vector from the X region. The entire third-zone Fermi surface lies near zone boundaries, but the neck region is nestled in the zone corner, and achieves near-contact with the second-zone surface. So it is not unnatural that the largest values of λ should occur there.

The results shown in Fig. 3 agree quite well with those of Leung (Ref. 7). As pointed out by him, the contrasting behavior between second and third zones (in the short-range variations) is not obtained in a *single*-OPW calculation, as done for example by Leavens and Carbotte.[8] The long-range variations, at least on the second zone, do seem to emerge correctly from such a treatment. This partial agreement between single-OPW and multi-OPW calculations is consistent with our interpretation of short- and long-range variations as 2-OPW and umklapp effects, respectively.

We compare calculated *orbital averages* of λ with those inferred from cyclotron resonance data

TABLE III. For the indicated Fermi surface points [see Figs. 1c and 2; U' is the point along arc AB of Fig. 2 whose velocity is vertical] we compare λ values measured by the surface-Landau-level method, with two sets of calculated values.

Point	λ(apparent), Refs. 9 and 13: Constant V_{ps}	λ(apparent), Refs. 9 and 13: E dependent V_{ps}	λ(calc): Ref. 7	λ(calc): Present work
X	0.49 ± 0.01	0.41 ± 0.01	0.41	0.42
L	0.46 ± 0.01	0.38 ± 0.01	0.39	0.37
U'	0.54 ± 0.02	0.45 ± 0.02	0.365	0.37

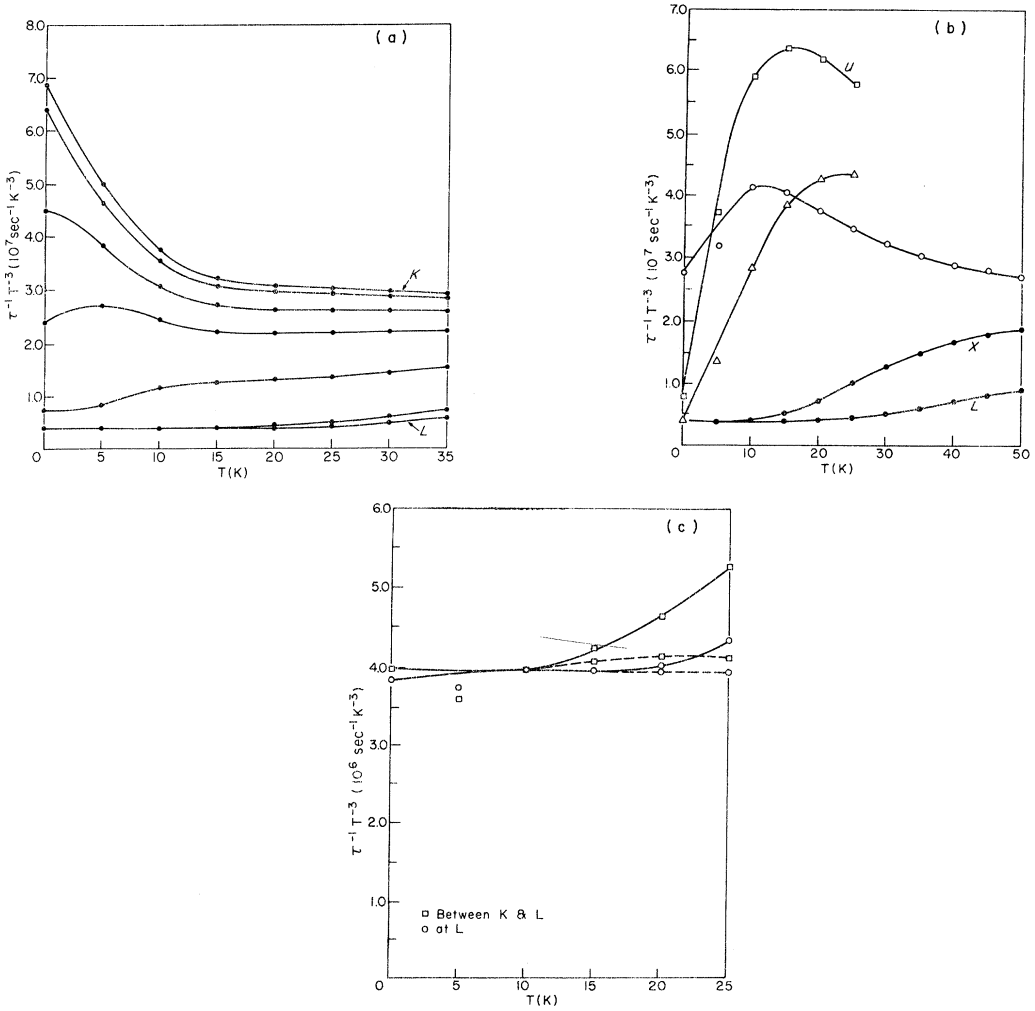

FIG. 4. (a) Plots of $\tau^{-1}T^{-3}$ as functions of temperature for points along second-zone segment KL, indicated on Fig. 1(c). Plots correspond in increasing order to points encountered as one moves from L to K. (b) Plots of $\tau^{-1}T^{-3}$ for points along segment LUX [again see Fig. 1(c)]. (c) Umklapp effect for point L and the point approximately midway between L and K. For each point, the lower part of the plot corresponds to the restriction of the integration (2) to the hexagonal face.

in Table II, and in Table III we compare calculated *point* values with the surface-Landau-level data obtained by Doezema and Wegehaupt.[9,13] In all but two cases (one of which has large experimental uncertainty), the agreement is very good. It is particularly pleasing that the anisotropies are in agreement. Note that in order to obtain close agreement, it was necessary to infer the "apparent" λ values by comparing observed effective masses with band masses calculated with account for the energy-dependence of the pseudopotential. The calculation is described by Ashcroft,[14] and his values appear in the fourth column of Table II. The same corrections have been applied in the second column of Table III.

B. Relaxation rates

We are interested in the scattering rate τ^{-1} as a function of both $\vec{k}$ and temperature T. Anticipating a T^3 dependence in free-electron regions, we plot $\tau^{-1}T^{-3}$ as a function of T (Fig. 4), for several points on the second-zone surface indicated on Fig. 1. At very low temperatures the anisotropy is huge. In free-electron regions there is an initial T^3 behavior which is augmented above a certain threshold by umklapp scattering. To show this we compare [Fig. 4(c)] the *total* scattering rate for points $\vec{k}$ in the hexagonal region, with that contribution which arises from scattering only to other states $\vec{k}'$ in the same hexagonal region (to eliminate umklapp).

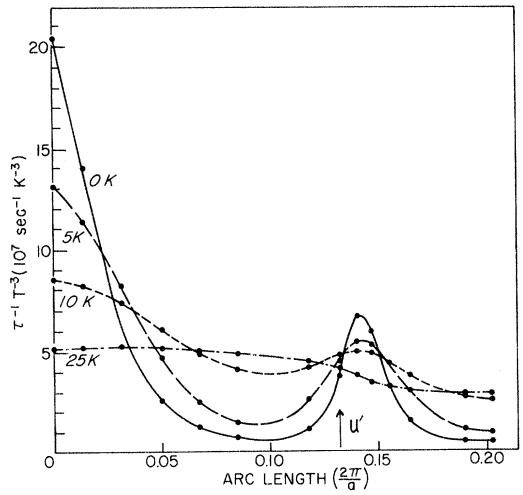

FIG. 5. Plots of $\tau^{-1}T^{-3}$ vs arclength on the (110) orbit of the third-zone arm (Fig. 2), for several values of the temperature.

Note that the umklapp onset temperature is reduced as the point $\vec{k}$ moves outward from the center (L) toward the zone boundary (K). Finally, as one approaches the ridge [Fig. 4(a)], there is no longer a well-defined umklapp threshold (the distinction between "normal" and "umklapp" is not always possible when 2-OPW states are involved); the quantity $\tau^{-1}T^{-3}$ starts out large and falls monotonically with increasing temperature. Viewed as a function of $\vec{k}$, $\tau^{-1}T^{-3}$ is sharply-peaked at ridges for low temperatures. As the temperature increases, the peaks broaden and the anisotropy washes out. The washing-out is accomplished by a reduction of $\tau^{-1}T^{-3}$ near ridges, accompanied by an increase in free-electron regions. This view is demonstrated in Fig. 5, where $\tau^{-1}T^{-3}$ is plotted as a function of $\vec{k}$, on the principal (110) orbit on the third-zone arm. The absence of flatness in the zero-temperature plot reflects the absence of completely free-electron character in the wave functions. It is not surprising that there is no apparent umklapp threshold.

The magnitudes of $\tau^{-1}T^{-3}$ are generally in good agreement with the measured ones (Table IV), particularly at the free-electron points X and L. The ranges of calculated values indicated for the third-zone point U' (shown on Fig. 5) and the third-zone orbit (Fig. 6) reflect the departures from purely cubic temperature dependence of τ^{-1}. These departures are untypically small, by comparison with those of third-zone points generally, and second-zone ridge points; this makes the U' point and the orbital average particularly appropriate for comparison with the data. The measured value associated with the U' point had previously been subject to ambiguous interpretation; it could equally well have been identified with the U point on the second zone[9] [see Figs. 1(c) and 4(b)]. However, a tipping study has led to the unique identification with U'.[13]

It would be interesting to confirm the predicted deviations from T^3 behavior. The most clear and easily interpreted ones occur on the second zone between L and K, as shown on Fig. 4(a). The $\vec{k}$ space variations are smoother near the V_2 ridges than near the V_1 ridges because the former have

TABLE IV. Measured and calculated scattering rates are compared for the same three points appearing in Table III, and, in addition, for the central arm orbit on the third zone. The ranges of calculated values indicated for the third zone apply to temperatures below 20 K. The departures from cubic behavior of τ^{-1} are evident in Figs. 5 and 6.

Point or orbit	$\tau^{-1}T^{-3}$ (10^7 $\mathrm{sec}^{-1}\mathrm{K}^{-3}$) Measured	Calculated [Eq. (5)]
Zone 2		
X	0.41 ± 0.03 [a]	0.40
L	0.39 ± 0.03 [a]	0.38
Zone 3		
U'	3.1 ± 0.3 [a]	3.8–5.0
(110) central arm orbit	4.0 ± 0.5 [b]	5.0–5.5

[a] Reference 9, surface-Landau-levels.
[b] Reference 2, Azbel'-Kaner cyclotron resonance.

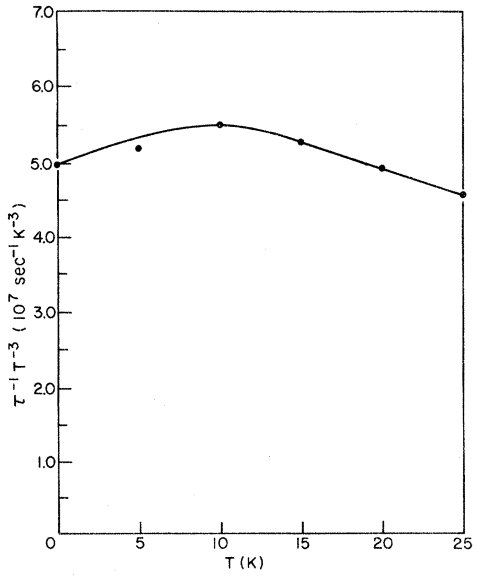

FIG. 6. The orbital average of $\tau^{-1}T^{-3}$ as a function of T, for the orbit of Fig. 5. The zero-temperature value is recorded in Table IV.

less curvature ($V_2 \sim 3V_1$).

In a few of the $\tau^{-1}T^{-3}$ plots [Figs. 4(b), 4(c)] there is a noticeable dip at 5 K, which results from the graininess of the mesh. Where it exists, the dip is small and there is nevertheless possible a smooth interpolation between $T=0$ and the $T \geq 10$ K points. With a finer mesh, the dip would occur at lower temperatures and be less pronounced. Because of practical calculational considerations, coupled with the limited availability of lifetime data, such an effort seems unwarranted at the present time.

IV. CONCLUDING REMARKS

The values of the effective-mass enhancements calculated here are consistent with those calculated previously by Leung,[7] even though the two calculations differ in their detailed treatment of electronic structure and in their methods of Fermi-surface integration. The calculated anisotropy exhibits the same trends found in both the surface-Landau-level data and cyclotron resonance data, and the actual magnitudes of λ agree closely in most cases. We have not calculated the entire Fermi-surface average of λ required for comparison with the specific-heat data, but Leung claims to have found fairly good agreement there.[15]

The agreement between measured and calculated scattering rates is pleasing. Agreement is particularly good at the X and L points, where because of the free-electron character of the wave functions, the T^3 coefficient depends on the form factor only at zero wave vector. Because of this it is not surprising that the coefficients are nearly the same at these two points. For the third zone (110)-orbital average, where τ^{-1} is nearly cubic in temperature, the agreement is quite good. There is some discrepancy, however, with the measured T^3 coefficient identified with the third-zone point U'. Owing to the rapid variations of $\tau^{-1}T^{-3}$ with both T and $\vec{k}$ near this point, one should perhaps not expect very close agreement for the U' point. Finally, the interpretation of data at such points would be facilitated if the predicted deviations from T^3 behavior were observed. Such observations would provide a stringent test of the theory, and, in particular, of the use of simple electronic structure for treating the electron-phonon interaction.

ACKNOWLEDGMENT

We would like to thank Professor R. E. Doezema for useful comments, and for access to his data prior to its publication.

---

*Work supported by the US ERDA through Grant No. AT(11-1)-2315.

†Present address: Dept. of Physics, Rensselaer Polytechnic Institute, Troy, N. Y., 12181.

[1]V. F. Gantmakher, Rep. Prog. Phys. 37, 317 (1974).

[2]R. E. Doezema and J. F. Koch, Phys. Kondens. Mater. 19, 17 (1975).

[3]J. W. Wilkins, *Observable Many-Body Effects in Metals* (Nordita, Copenhagen, 1968).

[4]P. B. Allen, in *Proceedings of the Twelfth International Conference on Low Temperature Physics, 1970* (Academic, Tokyo, 1970).

[5]See, for example, J. E. Robinson and J. D. Dow, Phys. Rev. 171, 815 (1968).

[6]N. W. Ashcroft, Philos. Mag. 8, 2055 (1963).

[7]H. K. Leung, Ph.D. thesis (McMaster University, Hamilton, Ontario, Canada, 1974) (unpublished).

[8]See C. R. Leavens and J. P. Carbotte, Solid State Commun. 9, 75 (1971), and references contained therein.

[9]R. E. Doezema and T. Wegehaupt, Solid State Commun. 17, 631 (1975).

[10]D. K. Wagner and R. C. Albers, J. Low Temp. Phys. 20, 593 (1975).

[11]N. W. Ashcroft, Phys. Lett. 23, 48 (1966).

[12]In the actual calculation, the momentum dependence of the form factor is accounted for by the addition of the term

$$\hat{\epsilon}_{q\sigma} \cdot \sum_{i<j} (\vec{G}_i - \vec{G}_j)\, 2\mathrm{Re}(\alpha_i^* \alpha_j)\, q \nabla_q V(\vec{G}_i - \vec{G}_j)$$

to (10a). This is omitted from the text for brevity.

[13]R. E. Doezema (private communication).

[14]N. W. Ashcroft, Ph.D. thesis (Cambridge University, 1964) (unpublished).

[15]Leung calculates the surface-averaged value $\lambda = 0.43$, which compares reasonably with the specific-heat value $\bar{\lambda}_{\mathrm{expt}} = 0.38$. See Ref. 7, and N. W. Ashcroft and J. W. Wilkins, Phys. Lett. 14, 285 (1965) for details.